Additive Manufacturing of Hierarchically Porous Silicon-based Ceramics: 3D Printing Black Glass with Unimodal, Bimodal, and Trimodal Porosity.

Ahmad R. Norouzi[a], Brett Paull[a,b], Vipul Gupta[a,b]*

[a]Australian Centre for Research on Separation Science (ACROSS), School of Natural Sciences, University of Tasmania, Hobart, Tasmania 7001, Australia

[b]ARC Centre of Excellence for Electromaterials Science (ACES), School of Natural Sciences, University of Tasmania, Hobart, Tasmania 7001, Australia

E-mail: vipul.gupta@utas.edu.au

Abstract

Silicon-based ceramics offer unique chemical and mechanical properties, gaining their hierarchically porous structures considerable attention over the years to advance various fields. Hence, a new resin system has been developed to precisely control the size and distribution of pores in silicon-based ceramics while allowing their high-resolution photopolymerisation-based 3D printing. The ability to control pore size and distribution of 3D printed ceramics by simply incorporating one or more of the above-mentioned resin components was explored by 3D printing silicon oxycarbide micro-structures, such as microneedles, with unimodal (micropores), bimodal (micro- and mesopores), and trimodal (micro-, meso-, and macropores) porosity. The resin system allowed precise modulation of pore sizes ranging from 1 nm to 200 nm and their three-dimensional distribution. Their elemental analysis suggested a total carbon content of 24.7% and an empirical formula of $SiO_{2.05}C_{1.06}S_{0.04}$*. The structures were found to be amorphous as per their X-ray diffraction.*

Silicon-based ceramics offer unique chemical and mechanical properties, such as chemical inertness, biocompatibility, significant strength, high glass transition temperatures, and high oxidative, creep, and crystallisation resistance [1]. These properties are further augmented by introducing micro- (< 2 nm), meso- (2-50 nm), or macro-pores (> 50 nm). Hence, their porous structures have received considerable attention over the years to advance various fields, such as catalysis [2-5], filtration[6, 7], extraction [8, 9], separation [10], sorption [11], energy production and storage [11-15], drug development [16-18], biomedical scaffolding [19, 20], sensors [21, 22], etc. Moreover, hierarchical or multi-level porosity structures are desired to achieve the required properties for these applications. These structures are inspired by natural elements, such as leaves, butterfly wings, and diatoms [3]. They are designed to enable structure and function properties, such as high accessibility, rapid transport of fluid and gases, high selectivity, fast uptake and release, rapid thermal cycling, chemical and mechanical stability, and efficient volume use [3]. For example, micro/mesopores provide the required surface area, and macropores provide the required chemical and mechanical stability,

convective heat transfer, turbulence, pressure drop, or external mass transfer for an application [23]. Hence, precise control of the micro-, meso-, and macro-porosity, along with the three-dimensional shape, size, and structure of a silicon-based ceramic component, is a fundamental capability.

However, porous silicon-based ceramics are primarily developed using soft or hard templates (including bio-templates), sol-gel processes, phase separation, or chemical etching. These methods are restricted to fabricating relatively simple structures and offer limited control over the percentage, type, and distribution of different pore sizes [3] . Moreover, these methods are not suitable for industrial applications because they are cumbersome and difficult to upscale [3]. The recent advent of 3D printing can offer new opportunities for fabricating these structures since they allow easy fabrication of complex and customised architectures and can be easily adapted for industrial applications because of their automated and environmentally friendly nature. However, 3D printing of porous silicon-based ceramics has been restricted to direct ink writing, which is intrinsically limited to the fabrication of low-resolution (>800 µm) and relatively simple objects[24] .Moreover, the developed resins lack any control over pore size and distribution. In 2019, DLP-based 3D printing was used for the first time to produce porous silica using a phase separating resin [25]. However, this approach also lacked any control over the pore size and distribution and was limited to only generating macro-pores (150 to 300 nm). These resins were composed of alkoxide inorganic precursors and organic binders, which also resulted in high linear shrinkage (>30%) because of relying on a high percentage of organic binders (> 50%), which were lost during pyrolysis.

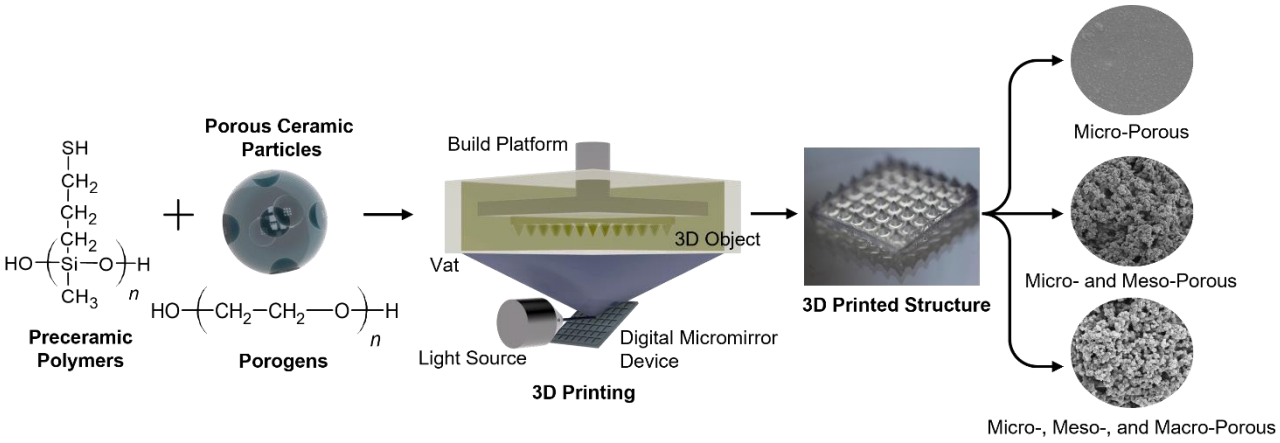

Figure 1. Schematic representation for 3D printing black glass with unimodal, bimodal, and trimodal porosity.

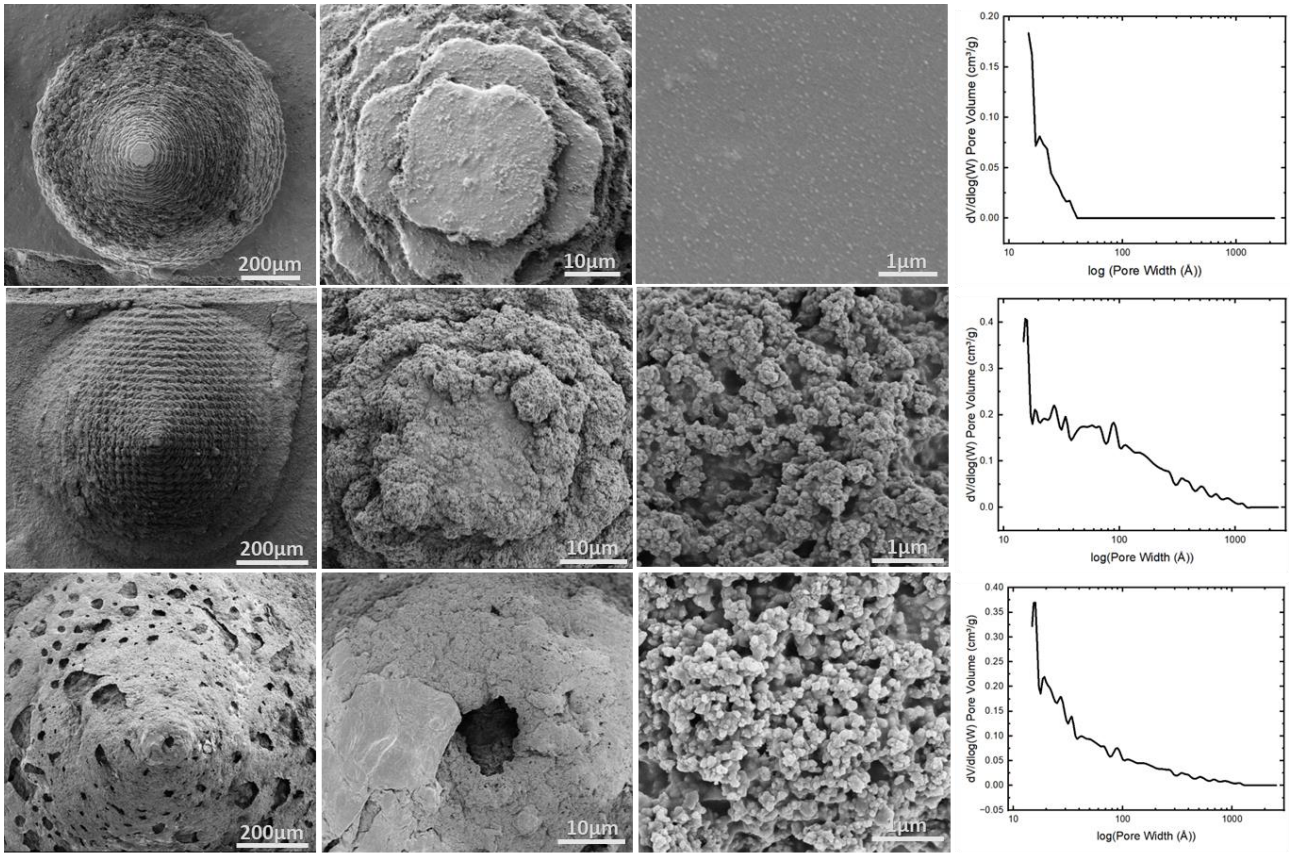

Figure 2. SEM images of the 3D printed microneedles in black glass with unimodal, bimodal, and trimodal porosity.

Structures with unimodal porosity can be 3D printed with a resin composed of porous ceramic particles with preceramic polymer binders. The preceramic polymer/s should be selected such that they do not result in any porosity upon pyrolysis into their respective ceramic. Hence, the resulting structural porosity can be pre-defined by the pore sizes of the ceramic particles. For example, as shown in Figure 2 (a), a microporous microneedle array was printed with a resin composed of mesoporous silica nanoparticles dispersed within (mercaptopropyl) methylsiloxane homopolymer and vinylmethoxysiloxane homopolymer. The resin resulted in a viscosity of 138.0 mPas, and a single-pixel resolution was obtained for the printing and pyrolysis of the resin (Figure 2 (aI and aII)). The use of two preceramic polymers with similar ceramic yields i.e., ca. 55% for (mercaptopropyl) methylsiloxane and ca. 50% for vinylmethoxysiloxane ensured their pyrolysis into non-porous ceramic, even at lower temperatures of 600 °C. A unimodal (micro) porosity was observed in the pyrolysed microneedles with an average pore size of 1.6 nm, a BET surface area of 357 m^2/g, and a pore volume of 0.12 cm^3/g (Figure 2 (aIII and aIV)). The resin resulted in a ceramic yield of 65% (Figure 3(a)) , and the pyrolysed structures observed a linear shrinkage of 15% as compared to their designed dimensions. Their elemental analysis suggested a total carbon content of 24.7% and an empirical formula of $SiO_{2.05}C_{1.06}S_{0.04}$ (Figure 3 (b)). The structures were found to be amorphous as per their X-ray diffraction (Figure 3 (c)).

Structures with bimodal porosity can be 3D printed with a resin composed of porous ceramic particles with low ceramic yield preceramic polymers. Low ceramic yield polymers pyrolyse into porous ceramics. However, the use of these polymers alone results in structural defects at

low pyrolysis temperatures. Hence, low ceramic yield polymers were used in conjunction with ceramic particles and high ceramic yield polymers to maintain the structural integrity of the printed objects. For example, as shown in Figure 2(b), bimodal micro- and meso-porous microneedle arrays were 3D printed with a resin composed of mesoporous silica nanoparticles dispersed within (mercaptopropyl) methylsiloxane homopolymer (ca. 55% ceramic yield) and methacryloxypropyl terminated polydimethylsiloxane (ca. 18% ceramic yield). A similar single pixel resolution was observed during printing and pyrolysis of this resin as above (Figure 2 (bI)). The use of a low ceramic yield polymer (methacryloxypropyl terminated polydimethylsiloxane) in equal weight proportion with a high ceramic yield polymer ((mercaptopropyl) methylsiloxane homopolymer) without any added particles did result in the desired structural integrity, however, it did not result in a bimodal porosity. The use of two preceramic polymers with significantly different ceramic yields in the presence of porous ceramic particles resulted in a micro- and meso-porous structure (Figure 2 (bII and bIII)). This is presumably because of the nucleation of ceramic growth around the ceramic particles, which resulted in meso-pores, while the porous particles contributed to the micro-pores. The pyrolysed microneedles resulted in pores ranging from 1.6 nm to 7 nm with a BET surface area of 524.7 m^2/g and a pore volume of 0.38 cm^3/g (Figure 2 (bIII and bIV)). The resin resulted in a ceramic yield of 35% (Figure 3 (a)), and post-pyrolysis, the printed structures resulted in a linear shrinkage of ca. 30%. The pyrolysed structures had a total carbon content of 26.61wt% with an empirical formula of $SiO_{2.01}C_{1.19}S_{0.004}$ (Figure 3 (b)) and were also found to be amorphous (Figure 3 (c)).

Structures with trimodal porosity can be 3D printed by incorporating a macroporous porogen in the above-mentioned bimodal porosity resin. The porogen should be selected such that it completely volatilises during pyrolysis. As shown in Figure 2 (c), trimodal micro-, meso-, and macroporous microneedles were 3D printed using a resin composed of porous ceramic particles, (mercaptopropyl) methylsiloxane homopolymer, and methacryloxypropyl terminated polydimethylsiloxane with 10% polyethylene glycol (PEG). A complete loss of PEG is observed at 500 °C, and it offers desired optical and rheological properties for DLP-based printing, making it a suitable candidate for 3D printing porous ceramics. The use of PEG 400 resulted in the introduction of macropores ranging from 50 to 200 nm, while the printing and pyrolysis process retained all the micro- and meso-pores obtained using the above-mentioned bimodal porosity resin. The pyrolysed microneedles resulted in a non-pixelated surface (Figure 2 (cI)) due to a decrease in the printing resolution owing to the presence of a non-photopolymerisable monomer (PEG) in the resin. The use of its photopolymerisable counterpart, polyethylene glycol diacrylate (PEGDA575) did not result in the generation of macropores as observed with the PEG, presumably because of its crosslinking with the preceramic polymers, preventing its phase separation and complete volatilisation during pyrolysis. The resin resulted in a ceramic yield of 30%, and the pyrolysed structures showed a BET surface area of 527.1 m^2/g, a pore volume of 0.3 cm^3/g, and 47.6% porosity (Figure 2 (cIII and cIV)). They observed a 30% linear shrinkage and were found amorphous with 25.7 % carbon content and an empirical formula of $Si_1O_{1.92}C_{1.02}S_{0.015}$(Figure 3).

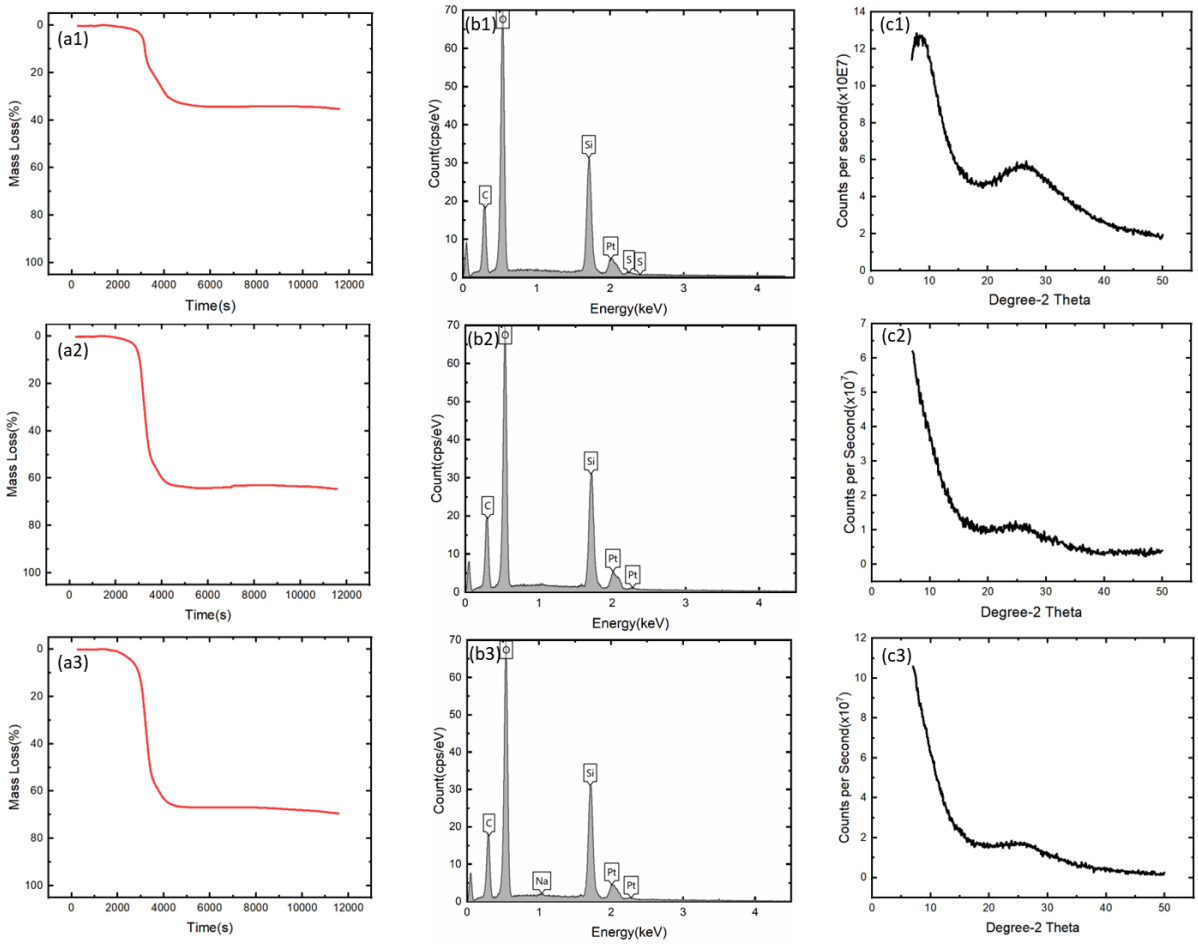

Figure 3. Material characterisation of the 3D printed unimodal, bimodal, and trimodal black glass and the respective resin: (a) thermogravimetric analysis of the resins, (b) elemental analysis of the printed structures, and (c) X-ray diffraction analysis of the printed structures.

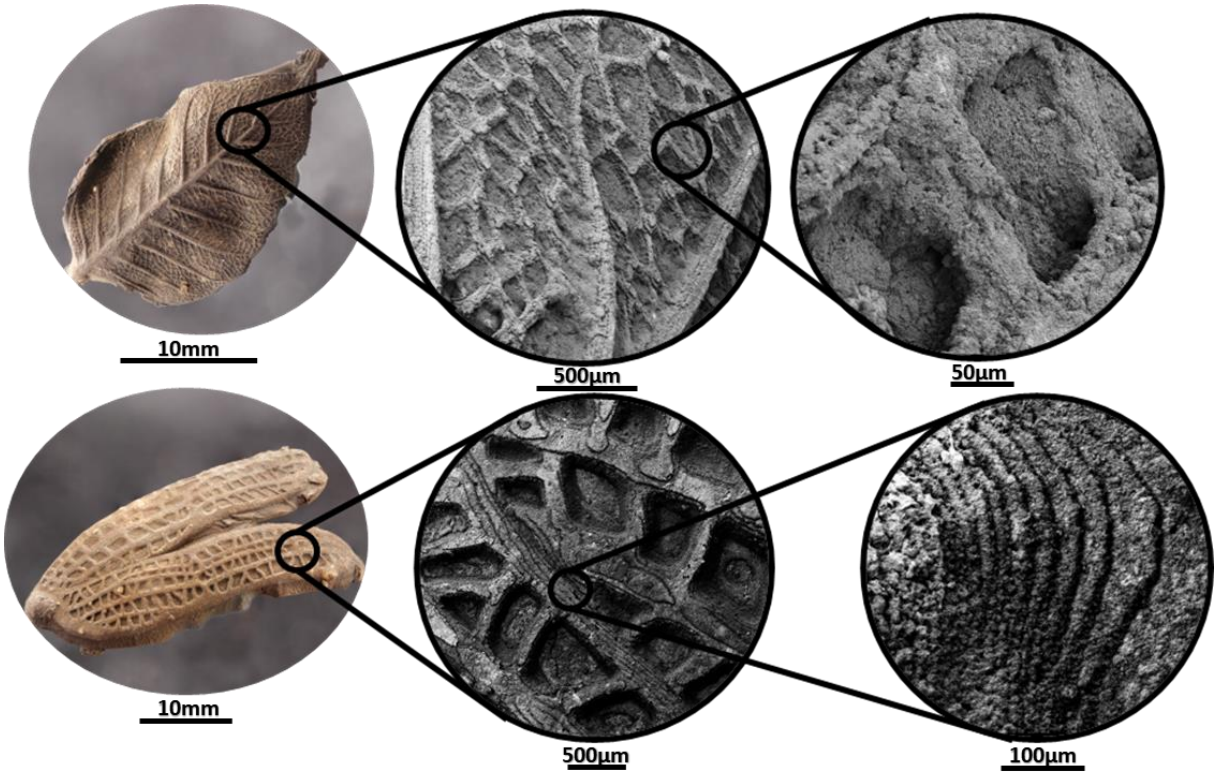

Figure 4. 3D printed replica of a hierarchically porous leaf (a) and insect wing (b).

The trimodal porosity resin (which offered the lowest resolution compared to other resins) was also studied to replicate naturally occurring hierarchically porous structures to further evaluate the potential of the method to 3D print high-resolution complex geometries and architectures with commonly used standard DLP-based printers. As shown in Figure 4 (a), a replica of the leaf was 3D printed in silicon oxycarbide while maintaining its external features, such as reticulate venation and ovate shape and internal multi-level porosity. Similarly, a replica of insect wings was 3D printed while maintaining the shape and structure of its cross veins and scales (Figure 4 (b)). These examples help visualise the resolution and potential of the developed resins and the printing and pyrolysis methods to produce silicon-based ceramic structures.

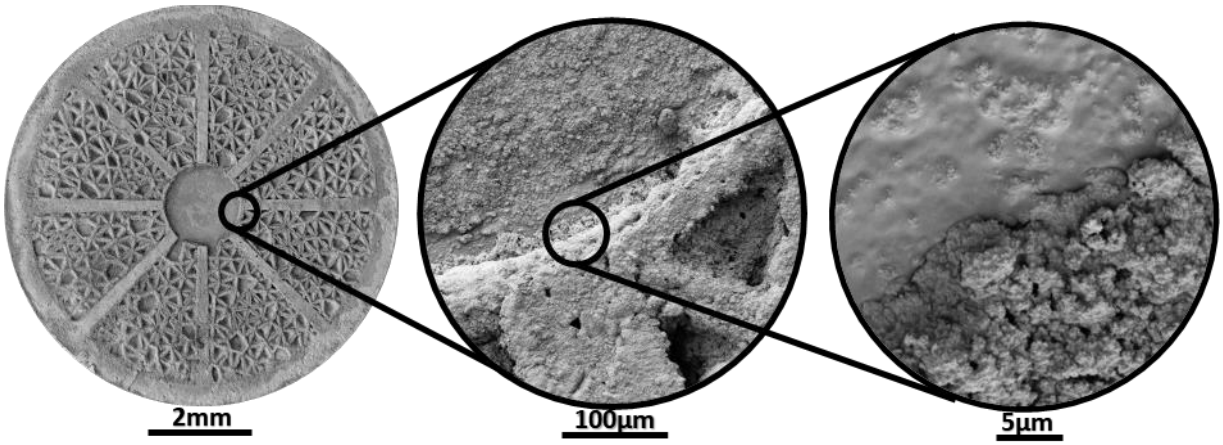

Figure 5. 3D printed replica of a diatom with bimodal valve and trimodal frustule.

The method was further extended to multi-material DLP-based printing since functional components usually require a combination of structures with different porosity levels. Again, 3D printing of a natural element, diatom, was studied. A replica of a centric diatom was developed with a cylindrical valve and a frustule containing interspersed areolae and slits (Figure 5 (a)). The model was 3D printed using a standard single-material DLP-based printer, where vats with different materials were interchanged between different layers by pausing and resuming the print as and when required. The valve was 3D printed with the bimodal porosity resin, and the frustule was 3D printed with the trimodal porosity resin. The pause and print method retained the high resolution of the DLP-based printer and did not result in any observable de-lamination between layers of different materials (Figures 5 (b and c)). The printed multi-material model's structural integrity and high definition were also maintained during pyrolysis (Figure 5 (b)). As shown in Figure 4 (c), SEM imaging clearly demonstrated the micro-, meso-, and macro-porous nature of the printed frustule and the micro- and meso-porous nature of the valve.

Conclusion

A new resin system has been developed to provide precise control over the size and distribution of pores in silicon-based ceramics while allowing their high-resolution photopolymerisation-based 3D printing. The resin comprises photo-polymerisable preceramic polymers, porous ceramic nanoparticles, and organic porogens. Different preceramic polymers and ceramic particles can be used to obtain binary, tertiary, or quaternary silicon-based ceramics, such as SiC, Si_3N_4, SiOC, SiCN, SiCNO, SiBCN, SiBCO, SiAlCN, SiAlCO, etc. The method was further extended to multi-material DLP-based printing since functional components usually require a combination of structures with different porosity levels. The pause and print method retained the high resolution of the DLP-based printer and did not result in any observable de-lamination between layers of different materials.

Experimental Section

Resin Characterisation

The photopolymerisation kinetics of the resins was studied using an attenuated total reflectance (ATR) based real-time Fourier-transform infrared (RT-FTIR) spectroscometer (Bruker Vertex 70, Ho Chi Minh City, Vietnam) in the range of 4000-600 cm^{-1}. A monochromatic UV LED with a 3 mm focusing lens (with λmax = 405 nm and intensity of 20 mW/cm2) (Digi-Key electronics) was used for photopolymerisation. A LED cover was custom designed and 3D printed to align the LED with the sample and to avoid samples being exposed to ambient light before experiments. The LED was positioned 3 mm above the ATR stage. The ceramic yield of the monomers and the resin were studied using a thermogravimetrical analyser (LABSYS, Bretagne, France) under nitrogen up to a temperature of 800 °C at a ramp rate of 10°C/min. The resin viscosity was studied using a digital viscometer (VISCO™, Tokyo, Japan) with 250rpm spinner rotation speed, and 30ml container with middle size spinner.

3D Printing

The structures were printed using a Miicraft Ultra50 3D printer (Young Optics Co., Hsinchu City, Taiwan). The printer uses a 365 nm projector and provides a 30 µm pixel size. A custom-designed resin tank (50 mm X 40 mm X 10 mm) with a 150 µm thick fluorinated ethylene propylene (FEP) film was used. The printed structures were cleaned in a IPA bath.

Microstructural Analysis

The 3D printed structures were visualised using a scanning electron microscope (Hitachi GmbH SU-70, Stoke Poges, United Kingdom) and a light microscope (Nikon Eclipse E-100 Trinocular Microscope, Victoria, Australia). For SEM imaging, the objects were sputter coated with Pt for 15 s, and the SEM micrographs were obtained using a 1.5-kV electron beam. The structural porosity was studied using a BET surface area analyser (Micromeritics TriStar II Plus, GA, USA) with nitrogen gas as the probe and a mercury porosimeter (Micromeritics, AutoPore™ IV, Caringbah, NSW,Australia). The elemental composition was studied with a flash elemental analyser (Thermo Finnigan EA 1112, Thermo Fischer, VIC, Australia) and energy-dispersive X-ray spectroscopy (Hitachi GmbH SU-70, Stoke Poges, United Kingdom). The crystallinity was studied using X-ray diffraction (Bruker D2Phaser Bragg-Brentano diffractometer) equipped with a Fe K-beta filter, divergence slit, incident- and diffracted-beam Soller slits of 2.5° and a LynxEye detector. The Co X-ray tube was operated at 30 kV and 10 mA.

References

1 Colombo, P., Mera, G., Riedel, R., and Soraru, G.D.: 'Polymer-derived ceramics: 40 years of research and innovation in advanced ceramics', Ceramics Science and Technology, 2013, pp. 245-320

2 Holland, B.T., Abrams, L., and Stein, A.: 'Dual templating of macroporous silicates with zeolitic microporous frameworks', Journal of the American Chemical Society, 1999, 121, (17), pp. 4308-4309

3 Su, B.-L., Sanchez, C., and Yang, X.-Y.: 'Hierarchically structured porous materials: from nanoscience to catalysis, separation, optics, energy, and life science' (John Wiley & Sons, 2012. 2012)

4 Su, B.-L., Sanchez, C., and Yang, X.-Y.: 'Insights into hierarchically structured porous materials: from nanoscience to catalysis, separation, optics, energy, and life science', Hierarchically Structured Porous Materials, 2012, pp. 1-27

5 Holland, B.T., Blanford, C.F., Do, T., and Stein, A.: 'Synthesis of highly ordered, three-dimensional, macroporous structures of amorphous or crystalline inorganic oxides, phosphates, and hybrid composites', Chemistry of Materials, 1999, 11, (3), pp. 795-805

6 Lorenz, M., Malangré, D., Du, F., Baune, M., Thöming, J., and Pesch, G.R.: 'High-throughput dielectrophoretic filtration of sub-micron and micro particles in macroscopic porous materials', Analytical and bioanalytical chemistry, 2020, 412, pp. 3903-3914

7 Silverman, L.: 'Filtration Through Porous Materials', American Industrial Hygiene Association Quarterly, 1950, 11, (1), pp. 11-20

8 Gao, Y., Sheng, K., and Wang, S.: 'Recent applications of organic molecule-based framework porous materials in solid-phase microextraction for pharmaceutical analysis', Journal of Pharmaceutical and Biomedical Analysis, 2022, pp. 115040

9 Delchet, C., Tokarev, A., Dumail, X., Toquer, G., Barré, Y., Guari, Y., Guerin, C., Larionova, J., and Grandjean, A.: 'Extraction of radioactive cesium using innovative functionalised porous materials', Rsc Advances, 2012, 2, (13), pp. 5707-5716

10 Zhang, J., Chen, J., Peng, S., Peng, S., Zhang, Z., Tong, Y., Miller, P.W., and Yan, X.-P.: 'Emerging porous materials in confined spaces: from chromatographic applications to flow chemistry', Chemical Society Reviews, 2019, 48, (9), pp. 2566-2595

11 Ippommatsu, M., Kurusu, C., Miyamoto, R., Ishii, S., Nakanishi, K., Minakuchi, H., and Yano, K.: 'Adsorption column for purifying body fluid', in Editor (Ed.)^(Eds.): 'Book Adsorption column for purifying body fluid' (Google Patents, 2010, edn.), pp.

12 Wu, L., Li, Y., Fu, Z., and Su, B.-L.: 'Hierarchically structured porous materials: Synthesis strategies and applications in energy storage', National science review, 2020, 7, (11), pp. 1667-1701

13 Kong, L., Zhong, M., Shuang, W., Xu, Y., and Bu, X.-H.: 'Electrochemically active sites inside crystalline porous materials for energy storage and conversion', Chemical Society Reviews, 2020, 49, (8), pp. 2378-2407

14 Chuhadiya, S., Suthar, D., Patel, S., and Dhaka, M.: 'Metal organic frameworks as hybrid porous materials for energy storage and conversion devices: A review', Coordination Chemistry Reviews, 2021, 446, pp. 214115

15 Li, Y., Fu, Z.Y., and Su, B.L.: 'Hierarchically structured porous materials for energy conversion and storage', Advanced Functional Materials, 2012, 22, (22), pp. 4634-4667

16 Carné-Sánchez, A., Carmona, F.J., Kim, C., and Furukawa, S.: 'Porous materials as carriers of gasotransmitters towards gas biology and therapeutic applications', Chemical Communications, 2020, 56, (68), pp. 9750-9766

17 Unger, K., Rupprecht, H., Valentin, B., and Kircher, W.: 'The use of porous and surface modified silicas as drug delivery and stabilising agents', Drug Development and Industrial Pharmacy, 1983, 9, (1-2), pp. 69-91

18 Qian, K.K., and Bogner, R.H.: 'Application of mesoporous silicon dioxide and silicate in oral amorphous drug delivery systems', Journal of pharmaceutical sciences, 2012, 101, (2), pp. 444-463

19 Varma, M.V., Kandasubramanian, B., and Ibrahim, S.M.: '3D printed scaffolds for biomedical applications', Materials Chemistry and Physics, 2020, 255, pp. 123642

20 Wang, X., Li, Y., Xiong, J., and Hodgson, P.D.: 'Porous TiNbZr alloy scaffolds for biomedical applications', Acta biomaterialia, 2009, 5, (9), pp. 3616-3624
21 Liu, Y., Guan, X., and Fang, Q.: 'Recent advances in AIEgen-based crystalline porous materials for chemical sensing', Aggregate, 2021, 2, (3), pp. e34
22 Wales, D.J., Grand, J., Ting, V.P., Burke, R.D., Edler, K.J., Bowen, C.R., Mintova, S., and Burrows, A.D.: 'Gas sensing using porous materials for automotive applications', Chemical Society Reviews, 2015, 44, (13), pp. 4290-4321
23 Yang, X.-Y., Chen, L.-H., Li, Y., Rooke, J.C., Sanchez, C., and Su, B.-L.: 'Hierarchically porous materials: synthesis strategies and structure design', Chemical Society Reviews, 2017, 46, (2), pp. 481-558
24 Putz, F., Scherer, S., Ober, M., Morak, R., Paris, O., and Hüsing, N.: '3D Printing of Hierarchical Porous Silica and α-Quartz', Advanced Materials Technologies, 2018, 3, (7), pp. 1800060
25 Moore, D.G., Barbera, L., Masania, K., and Studart, A.R.: 'Three-dimensional printing of multicomponent glasses using phase-separating resins', Nature materials, 2020, 19, (2), pp. 212-217